Acoustic Force Distribution in Resonators for Ultrasonic Particle Separation

Steven M. Woodside and James M. Piret
Biotechnology Laboratory and Dept. of Chemical and Bio-Resource Engineering, University of British Columbia, Vancouver, BC, Canada V6T 1Z3

Martin Gröschl and Ewald Benes
Institut für Allgemeine Physik, Technische Universität Wien, 1040 Wien, Austria

Bruce D. Bowen
Dept. of Chemical and Bio-Resource Engineering, University of British Columbia, Vancouver, BC, Canada V6T 1Z3

The effectiveness of particle–liquid separation by ultrasonic radiation forces depends on the acoustic energy density distribution in the standing-wave field. The energy distribution in an ultrasonic particle-separation device was analyzed to assist continued optimization and design efforts. Measurements of the energy-density distribution in the liquid using a microscope-based imaging system were compared to laser interferometer measurements of the velocity-amplitude distribution on the transducer and reflector surfaces of the ultrasonic separator. The energy density followed the same trend as the surface velocity, being highest near the resonator center and approaching zero near the walls. The energy density gradients and local gridlike reflector-amplitude variation had characteristic lengths of 1.4 mm. These results suggest that the energy-density distribution in the liquid is a defined function of the dimensions, imposed boundary conditions and physical properties of the reflector and transducer. This understanding provides a practical basis for developing a mathematical model of cell aggregation and retention, potentially enabling the design of resonators with predetermined energy density distributions for specific particle aggregation, separation, and fractionation applications.

Introduction

The capabilities of ultrasonic radiation forces for manipulating suspended particles have engendered a broad spectrum of experimental investigations. Ultrasonic aggregation has been exploited to improve the sensitivity of medical latex agglutination tests for detecting immunogenic agents (Grundy et al., 1994; Gualano et al., 1995), to fuse different cell types in combination with electric-field pulses (Vienken et al., 1985), and to enhance the recovery of two cell populations by phase partitioning (Allman and Coakley, 1994). The potential for continuous separation of particles from fluid suspensions was demonstrated by Tolt and Feke (1993). Continuous cell separation has been achieved for mammalian cells (Doblhoff-Dier et al., 1994; Trampler et al., 1994), yeast (Hawkes and Coakley, 1996), and bacteria (Hawkes et al., 1997). Fractionation according to particle size (Mandralis et al., 1994), continuous fractionation of mixed-particulate suspensions based on the compressibility of the solid phase (Gupta et al., 1995), and the selective retention of generally larger viable mammalian cells over nonviable cells and cell debris (Gaida et al., 1996) have been reported.

Particle separation by ultrasonic forces exhibits innate advantages relative to conventional methods, particularly in the area of biotechnology. Cross-flow membrane filtration and spin-filter separators suffer from fouling; continuous centrifuges are susceptible to mechanical failure; conventional sedimentation systems require long holdup times. For ultrasonic separation, no physical barrier is required, there are no

Correspondence concerning this article should be addressed to S. M. Woodside.

moving mechanical parts, holdup times are low, and chemical flocculants are not necessary. Trampler et al. (1994) demonstrated the advantages of ultrasonic separation, running a continuous mammalian-cell perfusion culture for more than one month at cell concentrations up to 6×10^7/mL, with no decline in separation performance.

In continuous separation systems, particles collect at the nodal planes of the standing-wave field due to the axial primary radiation force (PRF). Fluid flow is generally parallel to the nodal planes. The transverse PFR aggregates the particles within the nodal planes and retains them in the field against the flow-induced drag. The retention performance of these devices is therefore particularly dependent on the magnitude of the transverse PRF. The axial and transverse primary radiation forces are functions of the acoustic energy density (E_{ac}) distribution. Ultrasonic-force measurements by Woodside et al. (1997) showed that the E_{ac} in the ultrasonic field was highly nonuniform. Continued optimization and scale-up of ultrasonic retention devices will be assisted by improved knowledge of the ultrasonic force distribution and a better understanding of the mechanisms involved in generating this distribution. In this work, the relationship between the velocity amplitude distribution of the transducer and reflector surfaces, and the E_{ac} distribution in the liquid is examined. A heterodyne laser interferometer is used for the surface-amplitude measurements and a microscope-based imaging system for the liquid measurements. It is demonstrated that the properties and dimensions of the reflector and transducer are important in determining the energy distribution in the liquid, and hence the performance of the resonator.

Background

Primary radiation force

The PRF on spherical particles in an ideal fluid can be derived following the approach of Gor'kov (1962) for a standing-wave field of nonuniform oscillation-velocity amplitude, v_0, such that:

$$\boldsymbol{v}_{in}(x,y,z,t) = v_0(x,y,z)\cos(\kappa z)\cos(\omega t)\boldsymbol{k}, \qquad (1)$$

where κ is the wave number, ω is angular frequency, and $\boldsymbol{k}$ is the unit vector in the direction of the positive z-axis. Assuming that the z-dependence of v_0 is negligible relative to the variation of $\boldsymbol{v}_{in}$ over each wavelength, the time-averaged force can be described in terms of axial ($\boldsymbol{F}_z$) and transverse ($\boldsymbol{F}_{xy}$) components as

$$\boldsymbol{F}_z = -V_p E_{ac}\kappa(G_\rho + G_\beta)\sin(2\kappa z)\boldsymbol{k} \qquad (2)$$

and

$$\boldsymbol{F}_{xy} = V_p \nabla E_{ac}\left[G_\rho \cos^2(\kappa z) - G_\beta \sin^2(\kappa z)\right], \qquad (3)$$

where V_p is the particle volume, ∇ is the transverse gradient operator, and E_{ac}, the time-averaged acoustic energy density of the field, is

$$E_{ac} = 1/4\rho v_0^2. \qquad (4)$$

The density (ρ) and compressibility (β) acoustic contrast factors, given as

$$G_\rho = \frac{3(\rho_p - \rho_f)}{\rho_f + 2\rho_p} \qquad (5)$$

and

$$G_\beta = \left(\frac{\beta_f - \beta_p}{\beta_f}\right), \qquad (6)$$

respectively, define the influence of the fluid (f) and particle (p) properties on the acoustic forces. The axial PRF causes cells or solid particles to collect at the pressure-node planes of the standing-wave field. The transverse PRF aggregates such particles at the local E_{ac} maxima.

Ultrasonic resonator operation

A cross-sectional view of the ultrasonic resonance chamber is shown in Figure 1. The composite transducer (PSI Systems Inc., Canada) consisted of a 1-mm-thick, 2.5-cm-square PZT piezoelectric ceramic bonded to a 2.8-mm-thick Pyrex glass layer. The reflector was made of the same 2.8-mm-thick glass. The axial distance between the inner surfaces of the transducer and reflector was 23.70 mm $\pm$ 0.01 mm, and the chamber was 26×26 mm in transverse cross section. A standing plane-compression wave was produced in the chamber by supplying an alternating voltage signal across the plane electrodes of the piezoceramic at one of the resonance frequencies of the chamber. Resonance frequencies, f, between 2.1 MHz and 2.4 MHz, and their respective quality factors, Q, were determined from the electrical-impedance spectrum of the complete resonator following the procedure of Schmid et al. (1990). The closest resonance frequency to 2.25 MHz was selected as the operating frequency for all experiments, due to the high value of Q (up to 7,000) at that frequency. The average E_{ac} for the liquid volume was estimated (Burger et al., 1993) from the active power consumption, P, and the quality factor at the resonance angular frequency ω as:

$$E_{ac} = \frac{PQ}{\omega}. \qquad (7)$$

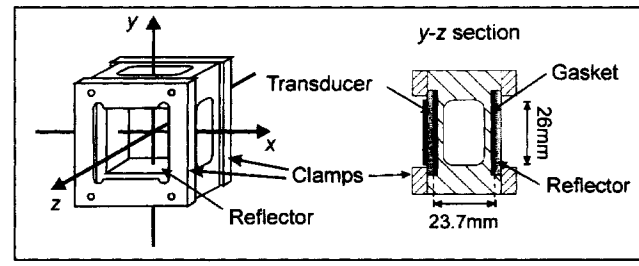

Figure 1. Resonator construction.

The transducer consists of a 1-mm-thick 25×25-mm piezoceramic bonded to a 2.8-mm-thick glass (32×32 mm in area). The reflector is composed of the same 2.8-mm-thick glass. The x-y cross-sectional area of the liquid volume is 26×26 mm.

Power consumption for the liquid-velocity amplitude measurements was determined from the on-line active power meter integrated with the ultrasonic power supply (PSI Systems Inc. USCS-04, Canada). The power consumption during the surface-velocity amplitude measurements was determined from the resonator impedance at the resonance frequency and the voltage amplitude across the piezoceramic transducer.

Liquid-velocity amplitude measurement

The ultrasonic force on 10.2-μm-diameter polystyrene particles was determined from the induced particle velocities using a microscope-based imaging system (Woodside et al., 1997) by assuming that each particle was at its terminal velocity and that the drag force was given by Stokes' law. The microscope field of view was approximately 1×0.7 mm, with a depth of view close to 0.2 mm. The axes are defined in Figure 1, with the origin at the symmetric center of the chamber. The measurement position in the experimental resonator was specified in three dimensions to ±0.05 mm using a micrometer-equipped stage. The average local E_{ac} was calculated from the best fit of the axial PRF model (Eq. 2) to the axial-force data. The oscillation-velocity amplitude of the liquid was calculated from the acoustic energy density (Eq. 4). The 95% confidence interval for the amplitude was determined from the standard error of the parameter fit.

Surface-velocity amplitude measurement

The nanometer-level displacement amplitude of an oscillating surface may be quantified based on the time-dependent interference between a constant-frequency reference beam and a frequency-modulated object beam (Eberhardt and Andrews, 1970; Thalhammer, 1993). The experimental apparatus used is depicted in Figure 2. A helium–neon laser beam (Spectra Physics 145 P, CA) of frequency Ω was divided at beam splitter A into a reference beam and an object beam. The reference beam was frequency shifted $\xi = 2\pi\cdot45$ MHz by the Bragg cell (Bragg cell and power amplifier, Intra Action ADM-40, IL; signal generator, Rhode & Schwarz SMS B4, Germany) and reflected by mirrors A and B, redirecting it to the photodiode (Texas Instruments TIXL 452, TX; Photodiode Power Supply Weir Minoreg P 325, Austria). Reflection of the object beam from the oscillating test surface produced a signal beam with a time-dependent Doppler-shifted frequency described by

$$\Omega' = \Omega + \Delta\omega\cos(\omega t), \tag{8}$$

where Ω' is the resultant frequency, $\Delta\omega$ is the Doppler-shift amplitude, and ω is the frequency of the test-surface oscillation. The reflected object beam was redirected toward the photodiode by beam splitter B and combined with the reference beam. The interference between these beams generated an intensity-modulated signal beam that was detected by the photodiode. The spectrum analyzer (Hewlett-Packard 3588A, TX) measured the frequency spectrum of the photodiode signal. The surface-displacement amplitude, a_0, was calculated from the ratio of the carrier-frequency (ξ) intensity to that of the first sideband ($\xi+\omega$). The time derivative of the surface

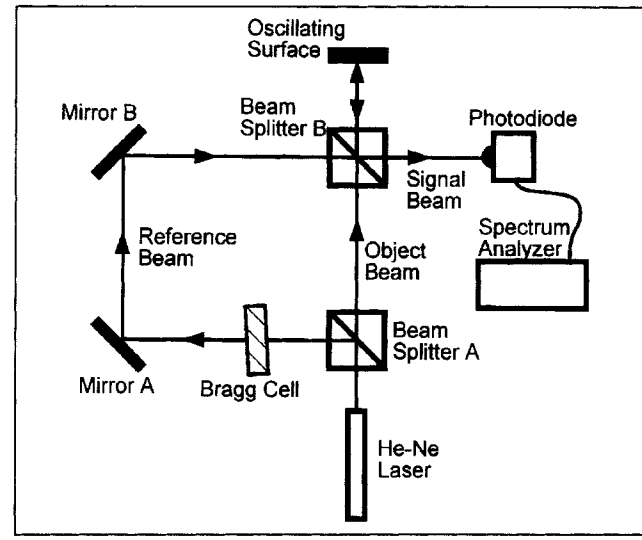

Figure 2. Laser interferometer.

The He–Ne laser beam is split into an object beam and a reference beam. The Bragg cell shifts the reference-beam frequency by $\xi = 2\pi\cdot45$ MHz. The reflected beam from the oscillating surface (angular frequency ω) is frequency modulated. The interference between the combined object and reference beams gives an intensity-modulated signal beam that is detected by the photodiode. The surface-oscillation amplitude is calculated from the intensity ratio of the carrier frequency (ξ) peak to the first sideband ($\xi+\omega$) as measured from the frequency spectrum of the photodiode output.

displacement,

$$a_s = a_0\sin(\omega t), \tag{9}$$

gives the surface velocity, that is,

$$v_s = \frac{da_s}{dt} = \omega a_0\cos(\omega t). \tag{10}$$

Surface-vibration amplitude measurements were performed on the transducer and reflector surfaces of the complete ultrasonic resonator (Figure 1). The outer electrode of the piezoceramic transducer was polished with an abrasive paste to produce a light-reflective surface. The reflector-glass surface was rendered reflective to light by vapor deposition of a chromium layer. The oscillation amplitude map of the surface was built up by scanning along one dimension of the measurement area and advancing incrementally in the other dimension after each traverse. Stepper motors (Spindler & Hoyer UT 100, Germany) controlled the translation of the sample in both directions. Scanning the 25×25-mm surface area of the ceramic with a 100-μm step size required 20 h. The optical table and damped pneumatic legs (Spindler & Hoyer X95, Germany) provided vibration isolation.

The power input to the resonator at a constant driving voltage is sensitive to slight changes in liquid temperature because of the high resonance quality factor. In the water-filled resonator a temperature shift of 0.01°C would cause a resonance-frequency shift of 100 Hz and a concomitant 10% drop in the input power at a constant driving voltage ($f = 2.25$

MHz, $Q = 5{,}000$). Ambient-temperature changes were greater than 1°C over the duration of a typical experiment. To maintain the temperature within ± 0.01°C for the duration of each measurement, water from a 4-L reservoir was circulated through the resonator (20 mL) at 12 mL/s using a centrifugal pump (RENA C20, France). The reservoir was temperature controlled to 25 ± 0.01°C in a water bath (Heto Lab Equipment CB13-25, Denmark).

Two-dimensional power spectral analysis

The surface-velocity amplitude data were acquired as a grid in the (x, y) spatial domains. The 2-D Fourier transform of these data to the wavenumber domain is a grid of complex coefficients representing the sinusoidal wave amplitude (real) and phase (imaginary) in two dimensions defined by the wave numbers κ_x and κ_y. The two-sided spectral power density was estimated by evaluating, at each grid point, the Fourier coefficient modulus divided by the grid area all squared. Waves of wave number $\kappa = (\kappa_x^2 + \kappa_y^2)^{1/2}$ travel in the direction $\theta = \sin^{-1}(\kappa_x/\kappa_y)$. The sound speed associated with each wave number was calculated using $c = \omega/\kappa$. The confidence intervals for the wavelength and sound-speed values were based on uncertainty bounds for the wavenumber equal to $\pm 50\%$ of the Fourier transform discretization interval.

Results and Discussion

The transducer surface-velocity amplitude distribution of the resonator is shown as a gray-scale map in Figure 3. Generally, the measured amplitudes were highest near the center of the ceramic ($x = 0$, $y = 0$) and fell toward zero at the edges. Local displacement amplitude maxima on the surface appeared as dark spots relative to the background and formed a gridlike pattern. The oscillation-amplitude map of a portion of the reflector surface is shown in Figure 4. The amplitude was again found to be highest near the center of the resonator and a gridlike pattern of localized amplitude maxima was discernible.

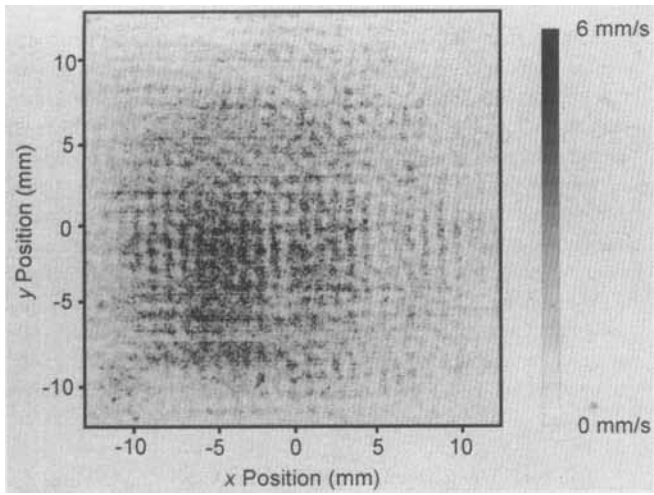

Figure 3. Piezoceramic-transducer surface-oscillation-velocity amplitude for resonator excited at $f = 2.244$ MHz, $P = 1.9$ W/L with $Q = 6{,}100$.

The oscillation amplitude is represented as a linear 128-level gray-scale map, with the regions of zero amplitude being white and those of amplitude 6.0 mm/s or greater appearing black. The data were acquired at 100-μm intervals, where the 25×25-mm measurement area encompassed the entire surface of the ceramic.

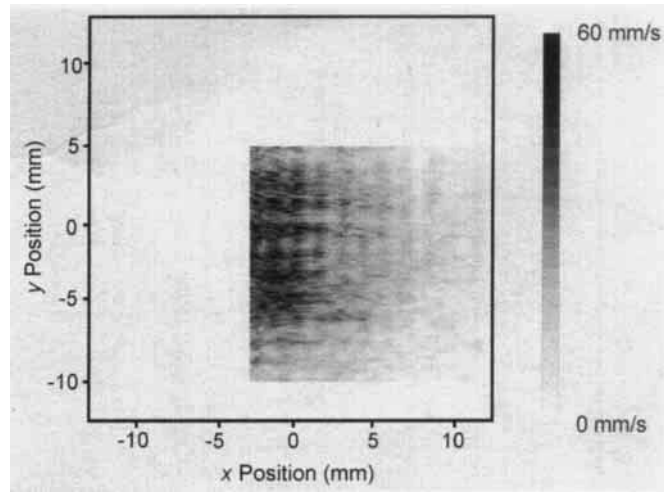

Figure 4. Glass-reflector surface-oscillation-velocity amplitude for resonator excited at $f = 2.251$ MHz, $P = 0.6$ W/L with $Q = 7{,}100$.

The x and y axes indicate the scale and position of the 15×15-mm measurement area relative to the measured area in Figure 3. The acquisition interval was 50 μm.

The liquid-oscillation amplitude, v_0, as a function of transverse position in the resonator was determined using the ultrasonic force measurement apparatus described by Woodside et al. (1997). Measurements were performed in the plane at the axial center of the resonator ($z = 0$). The liquid-vibration amplitude measurements as a function of x-position are plotted in Figure 5, with the surface-amplitude profiles of the reflector and transducer, at three transverse y positions. To permit a meaningful comparison between the different oscillation velocity data, they were normalized to $P = 30$ W/L and $Q = 5{,}000$. The abscissa velocity scales were selected to facilitate a visual comparison. The liquid-vibration amplitude was not measurable within 2 mm of the walls, that is, at $|x|$ or $|y| \geq 11.0$ mm; the normalized minimum detection level was approximately 85 mm/s. The error bars indicate the 95% confidence interval for v_0. The surface-amplitude profiles were produced by smoothing the data in Figures 3 and 4 using a centered 5×5 point-averaging kernel. The averaging area was thus 0.5×0.5 mm for the transducer and 0.25×0.25 mm for the reflector.

The liquid-vibration amplitude followed the same trend as the reflector amplitude, tending toward zero at the surface boundaries. However, an amplitude offset of approximately 3 mm/s was observed at the transducer boundaries. This offset was not attributable to random noise, as the mean amplitude of the unexcited transducer was a negligible 0.6 mm/s. The most plausible explanation is that in-plane oscillations at the driving frequency, combined with surface roughness on the scale of the incident-laser-beam diameter were detected as out-of-plane signals. This hypothesis is strongly supported by

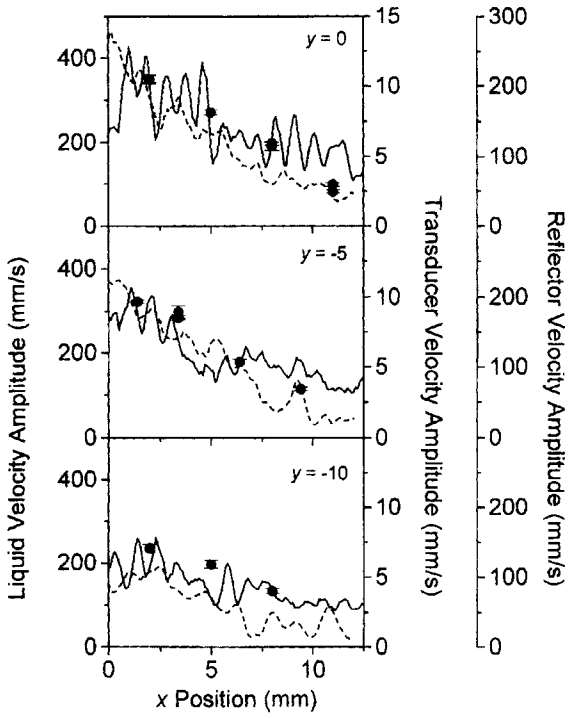

Figure 5. Oscillation amplitudes of transducer, reflector, and liquid.

The transducer amplitude (solid line) and reflector amplitude (dashed line) at ($y = 0$, -5 and -10 mm) calculated from the amplitude maps in Figures 3 and 4 are compared to liquid-oscillation amplitudes (filled circles) measured at approximately 3-mm increments along the x-axis, beginning near the center of the side wall (13.0, y, 0.0), and moving in toward the center of the resonator (0.0, y, 0.0). The velocity amplitude and hence the axial PRF are strongly dependent on transverse position in the resonator. All data are normalized to $P = 30$ W/L, $Q = 5{,}000$.

the following observations (data not shown): the location and the magnitude of high-amplitude outliers were reproducible; polishing the transducer electrode surface eliminated former outliers and created new ones; the reflector data did not exhibit a comparable offset, as this surface was prepared by vapor deposition and was thus significantly smoother.

The dependence of the liquid-oscillation-velocity amplitude on axial position in the field was examined in Figure 6. Sequences of experiments performed along two different lines parallel to the z-axis showed no discernible axial trend. As a consequence, the liquid-velocity amplitude distribution measured for the transverse plane $z = 0$ should be representative of the distribution in any other transverse plane. This finding, combined with the close correlation between the velocity amplitudes in the transducer, liquid, and reflector (Figure 5), suggests a functional relationship, dependent only on transverse position, between the liquid E_{ac} and the surface-amplitude distributions.

The one-dimensional model of an ultrasonic resonator developed by Gröschl (1998) predicts the acoustic energy densities and velocity amplitudes in the transducer, the fluid and the reflector from the material properties of each of these layers, and the voltage amplitude applied across the piezoceramic. The model was used to optimize the thickness of the

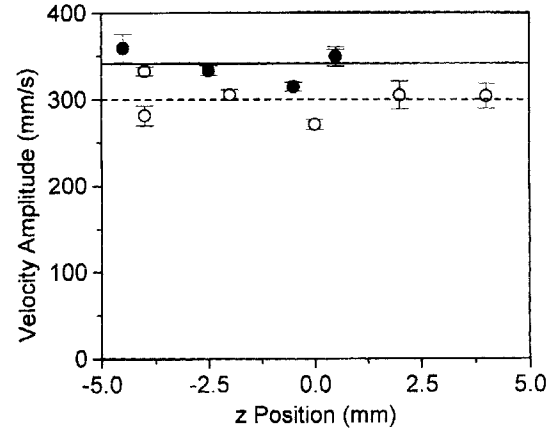

Figure 6. Axial variation of liquid-oscillation-velocity amplitude.

The results of measurements along the axis (2.0, 0.0, z) are plotted as solid circles; along (5.0, 0.0, z) they are plotted as open circles. The respective axial series averages are plotted as solid and dashed lines. All data are normalized to $P = 30$ W/L, $Q = 5{,}000$.

ceramic, glass, and liquid layers such that the acoustic-energy density (and hence the oscillation-velocity amplitude) was highest in the liquid. The utility of the model can be assessed by comparing the predicted and experimental velocity amplitude values.

The experimentally determined mean oscillation-velocity amplitudes for the reflector, transducer, and liquid layers of the resonator are listed in Table 1. The root mean square (rms) of the transducer-velocity amplitude was determined from the full data set presented in Figure 3. The rms of the reflector amplitude was calculated from the data in the area subtended by $y = 0$, $x = 12.5$, and $x = -y$ in Figure 4. It was assumed that the field was symmetric about these boundaries and that exclusion of the blank regions (less than 5% of the total area) had a negligible effect on the mean. The fluid-amplitude data in Figure 5, and additional data not shown, were acquired in the transverse plane $z = 0$ between the center and the side wall at approximately 3-mm intervals in the x-direction and at 5-mm intervals in the y-direction. The rms liquid-velocity amplitude was found by assuming that the amplitude at each point (x, y) was representative of the average over the region $x \pm 1.5$ mm and $y \pm 2.5$ mm and that the slight irregularity of the measurement grid was insignificant. It was further assumed that the field was symmetric about the plane $x = 0$ and that amplitudes below the level of detection were equal to zero. The zero-amplitude assumption would at most underestimate the rms liquid-velocity amplitude by 5 mm/s.

Table 1. Mean Oscillation-Velocity Amplitude Values Obtained from Measurements and 1-D Model Predictions*

Layer	Mean Layer Velocity Amplitude (mm/s)	
	Experiment	Model
Transducer	7.8	14
Liquid	190	170
Reflector	93	25

*$f = 2.251$ MHz; $P = 0.5$ W/L; $Q = 5{,}000$.

The model predictions in Table 1, normalized to $P = 30$ W/L and $Q = 5{,}000$, are consistent with the experimentally determined mean amplitudes. In both cases the transducer amplitude is the lowest, the reflector amplitude is intermediate, and the liquid amplitude is substantially higher. More significantly, the predicted and measured liquid-layer amplitudes are almost equivalent. Thus, the model would appear to be a valuable tool, both for estimating the mean E_{ac} in the liquid and for optimizing layer thickness such that the vibration amplitude is highest in the liquid. The divergence between the predicted and measured reflector amplitudes may be due to the sensitivity of the model to the compression-wave speed in the glass reflector. A 10% increase in wave speed from 5,430 m/s (used in the model) to 6,000 m/s results in a 200% increase in the predicted reflector amplitude because of the proximity of the operating frequency to the resonance frequency of the reflector, but has little effect on the transducer or liquid amplitudes. In any case, a one-dimensional model cannot predict the E_{ac} variation in the transverse direction. Characterization of the E_{ac} gradient distribution is essential to obtain mechanistic descriptions of particle aggregation and retention processes in separation systems that exploit the transverse PRF.

The spatial distribution of particle aggregates in the pressure-node planes was visualized using 3-μm-diameter alumina particles. The pattern formed by the aggregates (Figure 7) was most regular near the reflector and the periodicity was less pronounced in the y-direction, likely due to the effects of gravity. The average distance between adjacent columns of the larger aggregates was around 2.6 cm, with less distinct columns at 1.3-mm intervals. The distribution of aggregation loci is similar to the gridlike patterns of amplitude maxima in Figures 3 and 4. This suggests that the periodicity in the surface amplitude generates significant E_{ac} gradients in the liquid that contribute to the transverse PRF distribution.

Fourier analysis was employed to characterize the periodicity in the surface-amplitude data. The spectral power density of the transducer-surface-amplitude data is plotted as a gray-scale map in the upper part of Figure 8. The distinct circular pattern of radius $\kappa = 6{,}870$ m^{-1} corresponds to a standing-wave excitation with a wavelength of 0.91 ± 0.02 mm and a sound speed of $2{,}050 \pm 40$ m/s ($f = 2.244$ MHz). For the piezoceramic layer of the transducer, the transverse shear-wave speed is 2,100 m/s, while the transverse compression-wave speed is 4,100 m/s (Hoechst CeramTec specifications), suggesting that the detected amplitude pattern was due to the propagation of shear waves in the transverse plane of the ceramic. The dark points on the circle of radius $\kappa = 6{,}870$ m^{-1} at $\theta = 0$, $1/2\pi$, π, and $3/2\ \pi$ radians indicated high-amplitude waves propagating parallel to the edges of the ceramic. The grid pattern in Figure 3 was a result of the superposition of these waves. In the lower part of Figure 8 the relative power is plotted for the cross section of the map at $\kappa_y = 0$, showing the prominence of the peaks at $\kappa_x = \pm 6{,}870$ m^{-1} relative to the background.

The spectral power-density map of the reflector data demonstrated characteristic peaks at $\kappa_x = \pm 4{,}700$ m^{-1} as shown for the cross section at $\kappa_y = 0$ (Figure 9). The wavelength and sound speed of the corresponding standing wave are 1.36 ± 0.06 mm and $3{,}070 \pm 140$ m/s, respectively ($f = 2.251$ MHz). For Pyrex glass, a wave speed of 3,280 m/s has been reported for the shear wave and 5,640 m/s for the compression wave (Weast et al., 1986), again suggesting that the regular short-range variations in the surface-oscillation amplitude are due in part to surface shear waves.

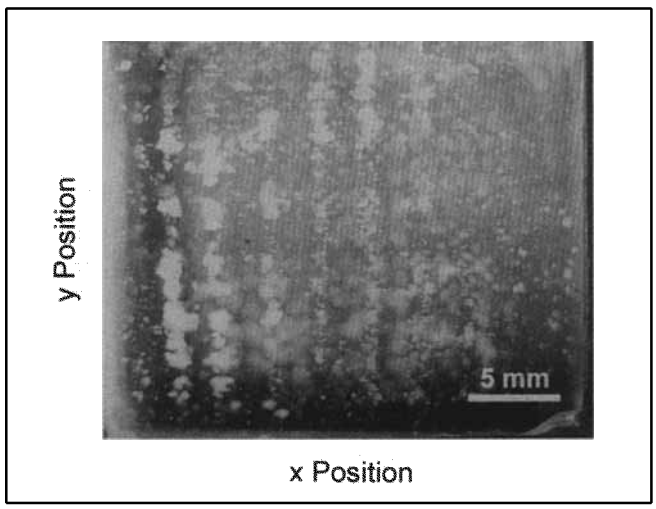

Figure 7. Aggregated 3-μm-diameter alumina particles at pressure-node planes.

The pressure nodes lie parallel to this x-y image plane. Aggregates are shown as seen through the glass reflector, looking toward the transducer, after $t = 10$ s of exposure to the standing-wave field.

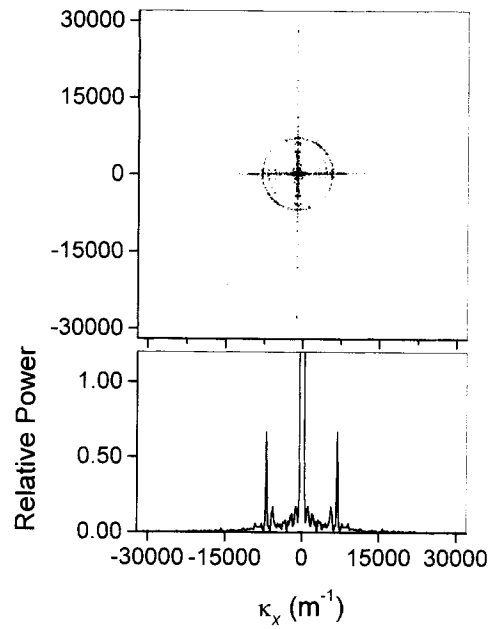

Figure 8. Spectral power density of the transducer-surface-velocity amplitude for the resonator excited at $f = 2.244$ MHz, $P = 1.9$ W/L with $Q = 6{,}100$.

The radius $\kappa = 6{,}870$ m^{-1} of the circle in the gray-scale power-spectral density map is consistent with the wave number of a standing shear wave propagating in the plane of the piezoceramic. The plot of relative power for the cross section at $\kappa_y = 0$ of the power-spectral-density map shows the prominence of the peaks at $\kappa_x = \pm 6{,}870$ m^{-1} relative to the background.

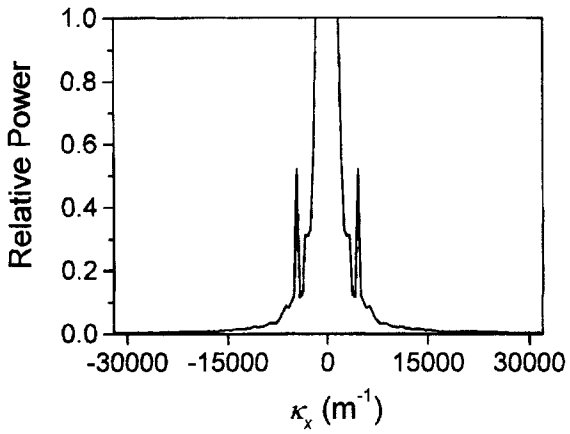

Figure 9. Spectral power density of the reflector-surface-velocity amplitude for the resonator excited at $f = 2.251$ MHz, $P = 0.6$ W/L with $Q = 7{,}100$.

The cross section at $\kappa_y = 0$ of the power-spectral-density map exhibits a strong excitation at $\kappa_x = \pm 4{,}700$ m^{-1}, consistent with a standing shear wave in glass.

The length scale of the transverse variations in liquid-oscillation amplitude was characterized by determining the positions of amplitude maxima and minima for different regions of the resonator. The trajectories of 10.2-μm-diameter polystyrene particles due to the transverse PRF served to identify the maxima and minima (Figure 10). Experiments were performed for a series of six adjacent pressure-node planes at two distinct transverse locations (Figure 11). The image sequence centered at (0, −7.5, 5.2) was not included because the observed trajectories in the two replicates were

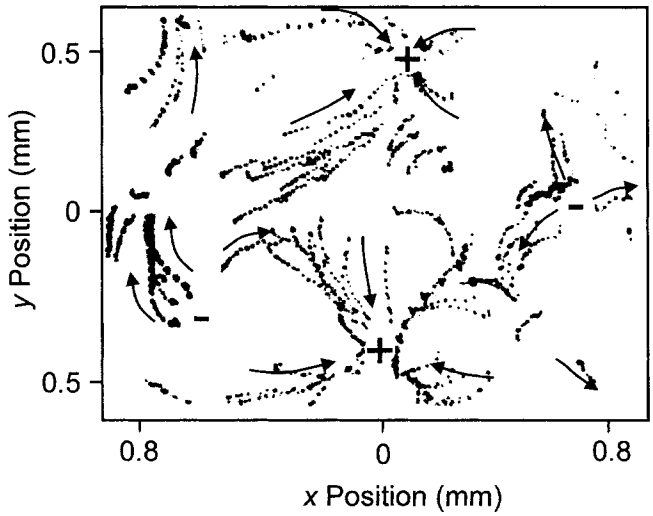

Figure 10. Trajectories of 10.2-μm-diameter polystyrene particles on a pressure-node plane due to the transverse PRF.

Superimposed sequential images acquired at 1-s intervals show the particle trajectories. Arrows indicate direction of particle motion in the 1.8×1.4-mm imaging area. Particles converge on the fluid velocity amplitude maxima (+) and diverge from the minima (−).

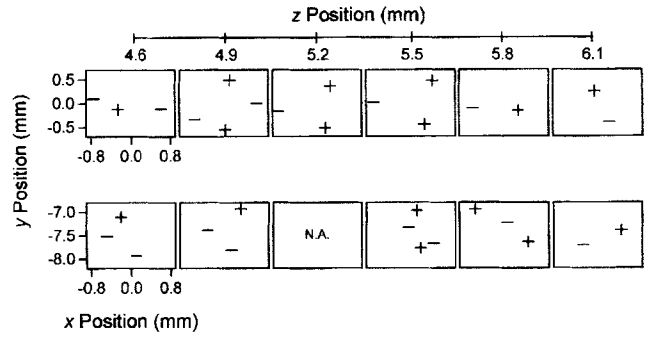

Figure 11. Positions of oscillation amplitude maxima (+) and minima (−).

The oscillation-velocity amplitude maxima and minima found on six adjacent pressure-node planes ($z = 4.6$ to 6.1 mm) are plotted for two experimental series centered on (0, 0, z) and (0, −7.5, z). The positions of the maxima and minima change from one nodal plane to the next. The frequency of occurrence remains approximately constant.

not comparable. The positions of the maxima and minima were found to vary between planes, in agreement with macroscopic observations that aggregates on adjacent planes are typically aligned at an angle from the axial direction. However, independent of the transverse location, the number of maxima and minima identified was approximately constant, with on average 1.5 each per 1.8×1.4-mm imaged area. Based on this frequency of occurrence, the expected distance between the maxima, assuming uniform amplitude variation in two orthogonal directions, is approximately 1.3 mm. This is essentially equivalent to the distance between adjacent maximum amplitude points on the reflector surface due to the surface shear wave.

The agreement between the characteristic length scale of the oscillation amplitude variation in the liquid and the shear wavelength on the reflector is likely due to energy transmitted to the liquid by these shear waves. Although the shear wave on the ceramic side of the transducer had a shorter wavelength (0.91 mm), this should not affect the length scale of the liquid-oscillation amplitude variation because only the glass side of the transducer was in contact with the liquid.

The length scale of the variation in the liquid-oscillation amplitude dictates the expected distance between aggregates. The magnitude of this variation dictates the strength of the E_{ac} gradients and thus the transverse PRF. The dependence of local E_{ac} gradients on transverse position was examined by measuring the maximum E_{ac} gradient at different points along the (0, y, 5.5)-axis using the transverse PRF measurement method of Woodside et al. (1997). The results in Figure 12 demonstrated that the maximum E_{ac} gradient was not as strong a function of transverse position as the E_{ac}. Thus, while the axial PRF falls from a maximum at the center to zero at the edges of each transverse plane, the maximum transverse PRF remains relatively high near the edge. The magnitude of the local E_{ac} gradients is likely more uniform throughout the resonator volume than the local E_{ac}, because the amplitude of the surface shear waves is approximately constant with transverse position.

The evidence that aggregates form across the entire transverse cross section of the resonator (Figure 7) is consistent

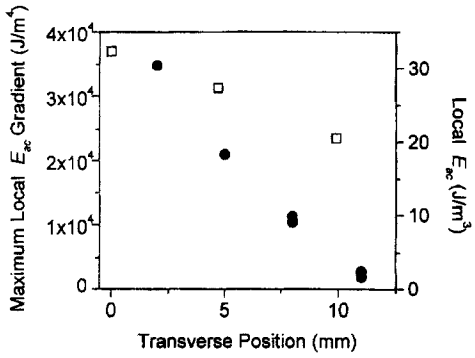

Figure 12. E_{ac} gradient in the liquid as a function of transverse position.

Local maximum E_{ac} gradient (open squares) is relatively constant with transverse position compared to the local average E_{ac} (filled circles). All data are normalized to P = 30 W/L, Q = 5,000.

with the findings in Figure 12. However, the 2.6-mm interval between the prominent bands of aggregates in Figure 7 appears to contradict the interval of 1.3 mm between the E_{ac} maxima observed in Figure 11. This factor-of-2 difference is postulated to be due to additional amplitude contributions from low-amplitude standing compression waves traveling parallel to the glass surface. Because the compression-wave speed is approximately double the shear-wave speed, the out-of-plane amplitude component from the response of the glass to compression would weaken the gradients near every second aggregation locus. A peak corresponding to this wave cannot be distinguished clearly in Figure 9 from the general low wave-number signal.

Conclusions

The E_{ac} distribution observed in the liquid can be ascribed to two distinct responses of the resonator to the excitation of the piezoelectric ceramic. The reflector and transducer behaved as though stationary boundary conditions for the axial plane compression wave were imposed along their edges, resulting in a field with high amplitude near the center and zero amplitude near the walls. The secondary excitation of the reflector and transducer glass, with surface shear waves propagating parallel to the edges, generated an important part of the local variations in E_{ac} that give rise to the transverse PRF. Thus, despite the low E_{ac} near the walls, ultrasonic particle separation remains effective as a result of the lesser change in the local maximum E_{ac} gradient with position in the resonator.

Generalizing for the case of a resonator of transverse dimensions l_x and l_y, and with a reflector and transducer shear-wave speed of c_s, the surface compression-wave amplitude contribution to the total liquid oscillation amplitude is expected to increase monotonically from zero near the walls ($\pm l_x/2$, $\pm l_y/2$) to a maximum near the center. Locally, the vibration amplitude should vary on the scale defined by the shear wavelength (c_s/f). The magnitude of this variation can be calculated as a first approximation from the measured local E_{ac} gradient maxima (Figure 12). This view of the E_{ac} distribution provides a simplified basis for modeling of particle aggregation and retention by ultrasonic forces, permitting the liquid layer to be approximated as a collection of regular volumes, each containing one E_{ac} maximum and one antinode plane. On this basis, the axial PRF on particles would be determined by the transverse position of the volume, while the transverse PRF distribution would be approximately equivalent for each volume.

The relationship demonstrated between the E_{ac} distribution in the liquid layer and the vibrational modes excited in the reflector and transducer may extend the capabilities for resonator design enabled by the one-dimensional resonator model. For example, the transverse PRF could be enhanced for separation processes by selecting conditions favoring the propagating of standing waves parallel to the solid–liquid interface in the transducer and reflector. More generally, by selecting the appropriate dimensions and materials, the resonator could potentially be designed to provide the appropriate E_{ac} distribution for specific applications.

Acknowledgments

The assistance of Rudolf Thalhammer, Bernhard Handl, and Hannes Böhm of the Institut für Allgemeine Physik, Technische Universität Wien in making the laser interferometric measurements is greatly appreciated. SW was supported by Natural Sciences and Engineering Research Council (NSERC) and BC Science Council GREAT scholarships. The work term in Austria was funded by the Canadian Government Going Global Program. We thank Felix Trampler at Psi Systems (Vancouver, BC) for valuable discussions.

Notation

G = acoustic contrast factor, dimensionless
$\boldsymbol{i}, \boldsymbol{j}, \boldsymbol{k}$ = unit vectors in x, y, z directions
t = time, s
v_{in} = velocity of incident acoustic wave, m/s
λ = wavelength, m

Literature Cited

Allman, R., and W. T. Coakley, "Ultrasound Enhanced Phase Partition of Microorganisms," *Bioseparation*, **4**, 29 (1994).

Burger, W., M. Gröschl, F. Trampler, and E. Benes, "Frequency Dependence of the Acoustic Loss Distribution in Piezoceramic/Liquid Resonators," *Proc. Ultrasonic Int. Conf.*, Butterworth-Heinemann, Oxford, p. 507 (1993).

Doblhoff-Dier, O., T. Gaida, H. Katinger, W. Burger, M. Gröschl, and E. Benes, "A Novel Ultrasonic Resonance Field Device for the Retention of Animal Cells," *Biotechnol. Prog.*, **10**, 428 (1994).

Eberhardt, F. J., and F. A. Andrews, "Laser Heterodyne System for Measurement and Analysis of Vibration," *J. Acoust. Soc. Amer.*, **48**, 603 (1970).

Gaida, T., O. Doblhoff-Dier, K. Strutzenberger, H. Katinger, W. Burger, M. Gröschl, B. Handl, and E. Benes, "Selective Retention of Viable Cells in Ultrasonic Resonance Field Devices," *Biotechnol. Prog.*, **12**, 73 (1996).

Gor'kov, L. P., "On the Forces Acting on a Small Particle in a Acoustical Field in an Ideal Fluid," *Sov. Phys. Dokl.*, **6**, 773 (1962).

Gröschl, M., "Ultrasonic Separation of Suspended Particles: I. Fundamentals," *Acustica*, **84**, 432 (1998).

Grundy, M. A., K. Moore, and W. T. Coakley, "Increased Sensitivity of Diagnostic Latex Agglutination Tests in an Ultrasonic Standing Wave Field," *J. Immunol. Methods*, **176**, 169 (1994).

Gualano, M. P., M. A. Grundy, W. T. Coakley, S. H. Parry, and D. J. Stickler, "Ultrasound-Enhanced Latex Agglutination for the Detection of Bacterial Antigens in Urine," *Br. J. Biomed. Sci.*, **52**, 178 (1995).

Gupta, S., D. L. Feke, and I. Manas-Zloczower, "Fractionation of Mixed Particulate Solids According to Compressibility Using Ultrasonic Standing Wave Fields," *Chem. Eng. Sci.*, **50**, 3275 (1995).

Hawkes, J. J., and W. T. Coakley, "A Continuous Flow Ultrasonic Cell-Filtering Method," *Enzyme Microb. Technol.*, **19**, 57 (1996).
Hawkes, J. J., M. S. Limaye, and W. T. Coakley, "Filtration of Bacteria and Yeast by Ultrasound-Enhanced Sedimentation," *J. Appl. Microbiol.*, **82**, 39 (1997).
Mandralis, Z., W. Bolek, W. Burger, E. Benes, and D. Feke, "Enhanced Synchronized Ultrasonic and Flowfield Fractionation of Suspensions," *Ultrasonics*, **32**, 113 (1994).
Schmid, M., E. Benes, and R. Sedlaczek, "Computer Controlled System for the Measurement of Complete Admittance Spectra of Piezoelectric Resonators," *Meas. Sci. Technol.*, **1**, 970 (1990).
Thalhammer, R., *Aufbau eines Heterodyn-Interferometers zur Messung von out-of-plane-Scwingungsamplituden*, Diplomarbeit, Institut für Allgemeine Physik, Technische Universität Wien (1993).
Tolt, T. L., and D. L. Feke, "Separation of Dispersed Phases from Liquids in Acoustically Driven Chambers," *Chem. Eng. Sci.*, **48**, 527 (1993).
Trampler, F., S. A. Sonderhoff, P. W. Pui, D. G. Kilburn, and J. M. Piret, "Acoustic Cell Filter for High Density Perfusion Culture of Hybridoma Cells," *Bio/Technol.*, **12**, 281 (1994).
Vienken, J., U. Zimmermann, H. P. Zenner, W. T. Coakley, and R. K. Gould, "Electro-acoustic Fusion of Erythrocytes and of Myeloma Cells," *Biochim. Biophys. Acta*, **820**, 259 (1985).
Weast, R. C., M. J. Astle, and W. H. Beyer, eds., *CRC Handbook of Chemistry and Physics*, CRC Press, Boca Raton, FL (1986).
Woodside, S. M., B. D. Bowen, and J. M. Piret, "Measurement of Ultrasonic Forces for Particle-Liquid Separations," *AIChE J.*, **43**, 1727 (1997).

Manuscript received Feb. 5, 1998, and revision received May 29, 1998.